Research Square

Preprints are preliminary reports that have not undergone peer review.
They should not be considered conclusive, used to inform clinical practice,
or referenced by the media as validated information.

High-Frequency Ground-Motion Simulation of the 2019 Ridgecrest Earthquake Using a k-2 Kinematic Source Model on a 3-D Non-Planar Fault and Empirical Green's Functions

Arpit Kumar Maurya
Indian Institute of Technology Roorkee
Simanchal Padhy
spadhy@es.iitr.ac.in

Indian Institute of Technology Roorkee

Research Article

Keywords: Empirical Green's Function, Kinematic Source Model, GMM, Ground motion simulation, source radiation, site-response

Posted Date: November 19th, 2026

DOI: https://doi.org/10.21203/rs.3.rs-11635760/v1

License: This work is licensed under a Creative Commons Attribution 4.0 International License.
Read Full License

Additional Declarations: No competing interests reported.

High-Frequency Ground-Motion Simulation of the 2019 Ridgecrest Earthquake Using a k^{-2} Kinematic Source Model on a 3-D Non-Planar Fault and Empirical Green's Functions

Arpit Kumar Maurya[1] and Simanchal Padhy[1*]

[1] Department of Earth Sciences, Indian Institute of Technology Roorkee, Roorkee, 247667, Uttarakhand, India .

*Corresponding author(s). E-mail(s): spadhy@es.iitr.ac.in;
Contributing authors: arpit_km@es.iitr.ac.in;

Abstract

Reliable simulation of near-source high-frequency ($>$ **1** Hz) ground motion requires accurate description of finite-source complexity together with path and site effects. We simulate 1–15 Hz ground motions of the 2019 $\boldsymbol{M_w}$ 7.1 Ridgecrest earthquake using a stochastic $\boldsymbol{k^{-2}}$ kinematic source on a non-planar 3-D fault coupled with radiation-corrected empirical Green's functions (EGFs). Twenty realizations of source were generated for each of the four stations spanning hard rock, soft rock, and alluvial sites. Simulated RotD50 PGA was compared with the BSSA14, CB14, and CY14 ground-motion models (GMMs). At the hard rock station CLC, PGA lies within a factor of about 1.4 of the GMM medians. At the soft-rock station CCC, it is approximately 1.5–1.7 times the medians for both EGF sets, consistent with its favourable position near the southern rupture end. At the distant hard-rock station GSC, PGA is systematically below the GMM median and shows the strongest sensitivity to EGF selection, whereas the PGA for the alluvial station SRT is below the GMM medians for both EGF sets. Bootstrap analysis suggests that selection of EGF has a dominant effect on PGA at the hard-rock stations CLC and GSC (Set 2/Set 1 ratios of 1.26 and 0.32, respectively) but not at soft-rock and alluvial stations SRT and CCC. The within-set residual standard deviations (0.30–0.56 in seven of eight cases) are comparable to or lower than those of the GMMs, and the pattern holds for all three GMMs. At hard- and soft-rock sites, the framework gives PGA consistent with the GMMs; basin sites require non-linear site-response analysis, however.

Keywords: Empirical Green's Function, Kinematic Source Model, GMM, Ground motion simulation, source radiation, site-response

1 Introduction

Simulation of earthquake ground motion at high-frequencies ($>$ 1 Hz) with detailed characteristics of the source, structure and site effect is important for the evaluation of seismic hazards (Campbell 2009). Source complexity, structure along the wave propagation path and local site conditions influence the resulting ground motion. Different approaches of ground motion simulation have been developed, including physics-based simulation (Ordaz et al. 1995; Graves 1996), empirical methods such as Empirical Green's Function (EGF) approach (Hartzell 1978), and hybrid

techniques (Kamae et al. 1998). Among these approaches, EGF method has developed significantly since Hartzell (1978) first proposed the use of small earthquake records as Green's functions to model large rupture events. Following this pioneering work, Irikura (1983, 1986) developed a semi-empirical EGF synthesis based on earthquake similarity and scaling relations between the source parameters of small and large earthquakes. Joyner and Boore (1986) further constrained the summation of small events using seismic scaling relations, while Irikura and Kamae (1994) extended the EGF technique to broad-frequency ground-motion simulation following the ω^{-2} source scaling.

There are approaches that incorporated EGFs into finite-fault kinematic models to represent the spatial and temporal evolution of rupture (Hutchings and Wu 1990; Hutchings 1994). The EGF method has been applied with the sub-fault dimensions scaled to the source parameters of the EGF event following the Irikura (1986) framework. This scaling helps to constrain the source parameters used in ground motion simulation (Asano 2018). In parallel, stochastic approaches used randomly time-shifted small-event records to reproduce the target ω^{-2} spectrum without requiring a detailed description of fault geometry and rupture dynamics (Wennerberg 1990; Ordaz et al. 1995; Kohrs-Sansorny et al. 2005). Causse et al. (2009) advanced this idea by coupling EGFs with a k^{-2} kinematic source model, producing broadband (0.1–30 Hz) ground motion synthetics for the Grenoble basin. The selection of an appropriate EGF is important in such simulations because differences in magnitude, focal mechanism, source location, alongside those in propagation path can influence the resulting ground motions (Del Gaudio et al. 2015). However, the point-source approximation used in the stochastic EGF approach does not explicitly account for finite-fault rupture directivity. This limitation was partially addressed by Wang et al. (2017) through an azimuth-dependent apparent corner-frequency correction to reproduce directivity effects, particularly at short periods. Beyond directivity, differences in focal mechanism between mainshock and EGF events can also affect the simulated ground motion (Nozu and Nagasaka 2017). Furthermore, conventional finite fault EGF implementations represent the rupture with a planar fault geometry and require the EGF event to be located near the sub-fault. This approximation becomes more restrictive for geometrically complex ruptures, where changes in fault orientation produce the azimuthal variation in the source radiation that cannot be fully reproduced. The sensitivity of EGF-based ground motion simulations to source radiation has thus been recognised as an important constraint.

Classical EGF applications generally require that small and target earthquakes have similar focal mechanisms in order to minimize source-mechanism differences (Shomali 2001). However, Del Gaudio et al. (2015) showed that significant near-fault variability can give rise to changes in radiation-pattern as rupture propagates over the fault. Dujardin et al. (2020) applied radiation-pattern correction to the EGFs to account for the spatial variability of source radiation. Their EGFs approximate actual Green's functions which have a unit seismic moment and flat amplitude displacement spectrum. We adopt here their combined k^{-2} source and radiation-corrected EGF framework to explain the observed site-specific ground motion variability in the source area of the 2019 Ridgecrest event, characterized by a geometrically complex rupture with a heterogeneous slip distribution.

The 2019 Ridgecrest earthquake occurred within the Eastern California Shear Zone, north of the Garlock Fault and approximately 150 km northeast of the San Andreas Fault (Wu et al. 2021). The sequence began on 4th July with an M_w 6.4 left-lateral foreshock, followed by a M_w 7.1 right-lateral mainshock on 6th July 2019 (Barnhart et al. 2019). The source of the 2019 event is characterized by hierarchical, interlocked orthogonal faulting across previously unmapped and immature fault segments (Ross et al. 2019) and revealed geometrically complex surface ruptures near the mainshock (Wang and Zhan 2020). The roughness of fault surfaces, along with the structural complexity play a significant role in rupture propagation. Kinematic inversion of the 2019 mainshock constrained by joint analysis of strong motion records, high-rate GNSS, and teleseismic waveforms reveals a complex rupture history characterized by heterogeneous slip distributions and highly variable rupture behaviour (Chen et al.

2020; Jia et al. 2020; Wang et al. 2020). These characteristics make the Ridgecrest mainshock an appropriate case for examining how a non-planar fault geometry and heterogeneous rupture process describe near-source high-frequency ground motion variability.

To apply the aforementioned simulation method Dujardin et al. (2020) to the 2019 Ridgecrest mainshock, a 3-D non-planar fault geometry with spatially varying strike and dip was used to represent the along-strike and depth-dependent curvature of the rupture. Multiple stochastic source realizations were generated by varying the source parameters that control the finite-fault rupture. Two independent EGF sets were used to examine the sensitivity of the simulated ground motion to EGF selection. Before finite-source summation, the EGFs were corrected for differences in travel time, geometrical spreading, anelastic attenuation, and radiation pattern. The simulated RotD50 PGA was evaluated against the recorded motions and the median predictions of three NGA-West2 ground-motion models, BSSA14, CB14, and CY14. Natural-log residuals, paired-bootstrap statistics, and residual–distance correlations were used to quantify the station-dependent simulation behaviour and the influence of EGF selection. Finally, we evaluated the performance of the k^{-2}-EGF framework for contrasting source-to-site conditions and examined the extent to which EGF selection and finite-source variability contribute to uncertainty in site-specific high-frequency ground-motion evaluation.

2 Data

In this study, we used the 2019 Ridgecrest event dataset of Trugman (2020) from the Southern California Earthquake Data Center (SCEDC). It contains a subset of 55 events, including aftershocks following the mainshock occurred between 04 July 2019 and 17 July 2019. These events have magnitude in the range 2-4. The events are recorded at 65 stations across five different seismic networks. This study focuses on Southern California seismic network stations located at different lithologies. The earthquake sequence was recorded at stations with different site conditions, characterized by V_{s30}. The stations used in this study, located on soft rock, hard rock, and alluvium are shown in Figure 1 along with the selected EGF events. The V_{s30} values are provided by the Strong Motion Data Centre (see Data and Resources).

2.1 Station Selection and Site Characteristics

We have selected four stations with different lithologies based on their Vs30 values (see Table 1) (Yong et al. 2016). Stations CLC and GSC are situated on hard rock (granitic rock). CLC is close to the mainshock located only 5 km to the north (Ahdi et al. 2020), while GSC is located much farther away about 90 km to the southeast (Figure 1). Station CCC is located on a soft rock site close to the mainshock, while SRT is an alluvium site (Figure 1).

Table 1 List of seismic stations used in this study.

Station Code	Latitude	Longitude	V_{S30} (m/s)	Site Class
CLC	35.8157° N	117.5975° W	1464	B
GSC	35.3018° N	116.8057° W	697	C
CCC	35.5249° N	117.3645° W	432	C
SRT	35.6923° N	117.7505° W	301	D

2.2 EGF Selection

From a set of 55 events comprising the dataset of Trugman (2020), we selected those events that are close to the mainshock and share the same path and site effects. We have selected two sets of events (set-1 and set-2), each set containing three EGFs (Table 2 and Figure 1). The events are selected based on the following criteria: (1) The EGF hypocentre is located close to the mainshock, (2) the event moment magnitude is greater than 3.5, and (3) the event is recorded at all the target stations.

The first event in set-1 (M=3.84) occurs on July 06, 2019 and is located close to the mainshock, while the first event (M=3.98) in set-2 occurred on July 06, 2019 and is located around 16 km from the mainshock. The second event in set-1 (M= 3.90) occurred on July 06, 2019 and is located nearly 19 km from the mainshock, while the second event in set-2 (M=3.98) struck on July 07, 2019 and is located nearly 2 km from the

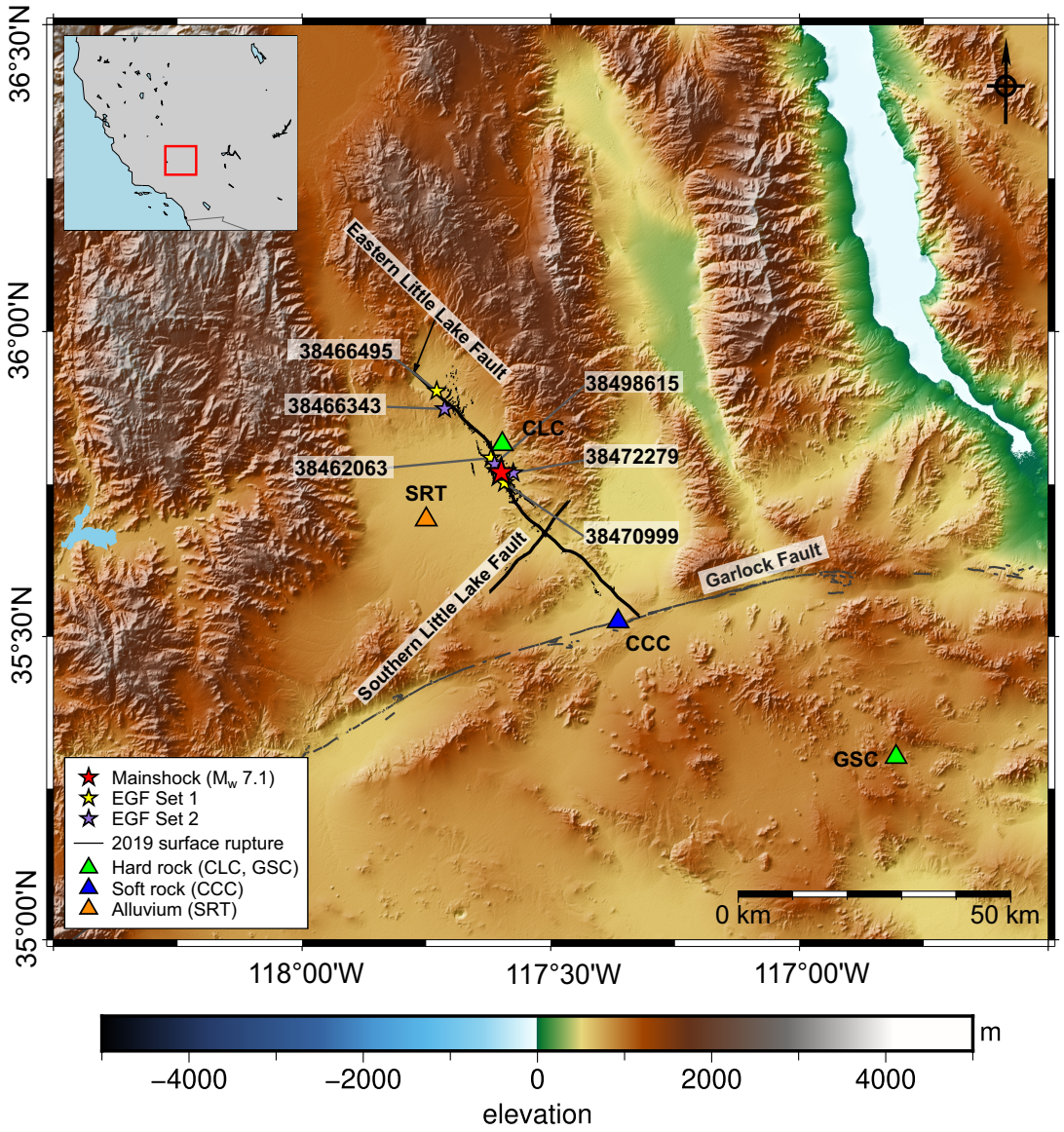


Fig. 1 Seismotectonics map of the study area showing the 2019 M_w 7.1 Ridgecrest mainshock, selected empirical Green's function (EGF) events, recording stations, and major fault structures. The Eastern Little Lake and Southern Little Lake faults are shown as solid black lines extracted from the SCEC Community Fault Model (CFM5; Plesch et al. 2020); the 2019 surface ruptures mapped by the California Geological Survey (CGS) are represented by thinner black lines. The Garlock fault is shown as a dark-grey dashed line. The mainshock is indicated by a red star, while EGF events from Set 1 and Set 2 are represented by yellow and purple stars, respectively, and labelled with their SCEDC event IDs. The recording stations are shown as triangles classified by site conditions: hard rock (CLC and GSC; green), soft rock (CCC; blue), and alluvium (SRT; orange). The inset shows the location of the study area within California. Background topography is shown as shaded relief, with elevation (in m) indicated by the color scale at the bottom.

mainshock event. The 3rd event in set-1 (M=3.62) occurred on July 07, 2019 and is very close to the target event, while the 3rd event in set-2 that occurred on July 09, 2019 is very close to the mainshock.

The entire dataset is pre-processed as follows: (1) instrument response removed, (2) demeaned and detrended, (3) cosine-tapered, and (4) band-pass filtered between 1 and 15 Hz. The low-frequency cutoff is based on the signal-to-noise

Table 2 Source parameters of the EGFs.

Event	Latitude (°N)	Longitude (°W)	Depth (km)	Strike (°)	Dip (°)	Rake (°)	M	M_0 (N m)	f_c (Hz)
Set 1									
38462063	35.793	117.620	5.524	351	30	−77	3.84	4.412×10^{14}	5.06
38466495	35.902	117.729	4.6	349	87	−167	3.90	6.602×10^{14}	3.71
38470999	35.752	117.593	11.1	334	79	−159	3.62	4.426×10^{14}	5.61
Set 2									
38466343	35.873	117.713	8.049	110	88	−154	3.98	5.012×10^{15}	1.68
38472279	35.768	117.575	10.530	327	42	−168	4.52	4.276×10^{15}	3.10
38498615	35.783	117.613	9.09	230	21	−118	3.58	2.724×10^{14}	5.31

Note: M is the Southern California Seismic Network (SCSN) catalog preferred magnitude (2020). Locations are taken from Trugman (2020).

ratio (SNR), which is calculated from 10 s signal window, starting at 5% of the Arias intensity. The normalised cumulative Arias intensity (Husid function) of the record is used as an objective, energy-based picker of the S-wave onset, since its 5% level consistently marks the transition from the low-energy P-coda to the S-wave arrival. This level is compared against a preceding 10 s noise window taken before the P-wave arrival. The amplitude spectra are smoothen using the Konno and Ohmachi (1998) algorithm. We fixed SNR above 5 for data selection (Figure 2). Also, the EGFs time series were also visually inspected to assess the quality of the recordings and identify any anomalous waveform characteristics (Figure S1).

3 Methodology

We review here the major components of the methodology of Dujardin et al. (2020) that is adapted here for ground motion simulation.

A k^{-2} kinematic source model is assumed for the M_w 7.1 Ridgecrest earthquake, as proposed by Herrero and Bernard (1994). Following the Brune source model (Brune, 1970), theoretical corner frequency is calculated using stress drop ($\Delta\sigma$), seismic moment (M_o) and shear wave velocity V_s as:

$$f_c = \left(\frac{16\Delta\sigma}{7M_o}\right)^{1/3} kV_s, \tag{1}$$

where k is a constant having a value of ∼0.37. The corner wavenumber, k_c is expressed as reciprocal of rupture duration, T_{Rup} (Hanks 1979):

$$k_c = \frac{1}{T_{\mathrm{Rup}}} = \frac{V_R}{D_{\mathrm{Rup}}} = \frac{f_c}{V_R}, \tag{2}$$

where V_R is the rupture velocity and D_{Rup} is the characteristic rupture size defined by $D_{\mathrm{Rup}} = \sqrt{L^2 + W^2}$, where L and W are the length and width of the rupture area, respectively. Stress drop is used to constrain the ground motion variability. Slip is set at its mean estimate taken over the low-frequency part of the rupture area, $\bar{D}$ and is calculated using the relation as:

$$M_o = \mu A \bar{D}, \tag{3}$$

where A is the rupture area defined by $L \times W$ and μ is the rigidity expressed as $\mu = \rho V_s^2$ ($\rho = 2.8$ g/cm^3). The heterogeneity in slip distribution at high frequency follows asymptotic decay as k^{-2} beyond corner wavenumber and is defined as (Herrero and Bernard 1994):

$$D(k_x, k_y) = \frac{\bar{D}\, LW}{\sqrt{1 + \left[\left(\frac{k_x}{k_{cx}}\right)^2 + \left(\frac{k_y}{k_{cy}}\right)^2\right]^2}}\, e^{i\phi(k_x, k_y)}, \tag{4}$$

where k_x and k_y represent wavenumber along the strike and dip directions, respectively. The term $\phi(k_x, k_y)$ represents a randomized phase spectrum, while k_{cx} and k_{cy} define the corner wavenumbers for strike and dip, respectively.

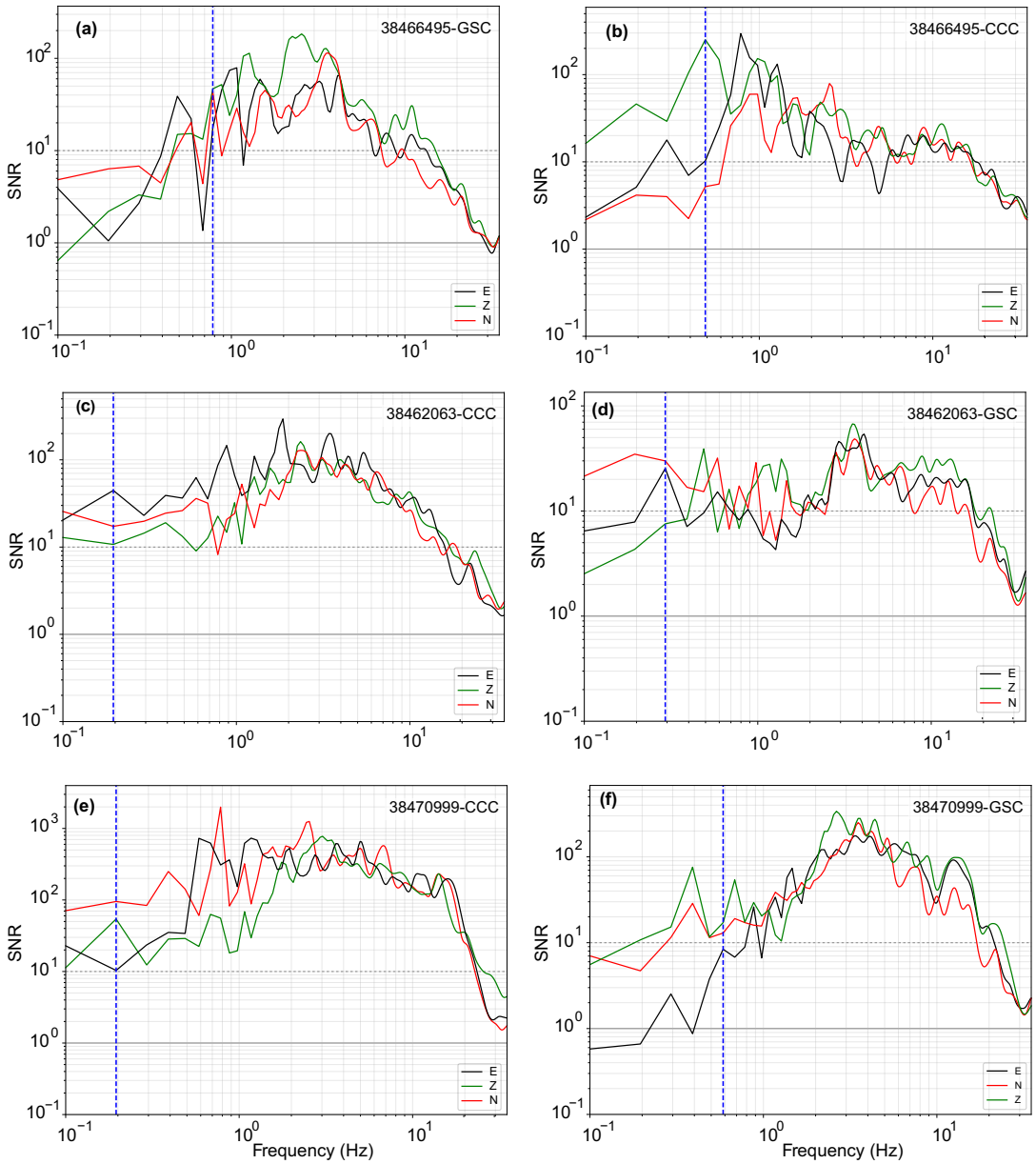


Fig. 2 Frequency-dependent Signal-to-noise ratio (SNR) shown for the Set 1 EGFs. The three-component (Z, N, and E) data recorded at the GSC hard rock site (a, c, e) and the CCC soft rock site (b, d, f) are plotted using different colours. The low-frequency threshold (SNR < 5) is indicated by the dashed blue line. The limit is identified at 0.78 Hz (a), 0.48 Hz (b), 0.29 Hz (c), 0.20 Hz (d), 0.58 Hz (e), and 0.19 Hz (f).

3.1 Spatial Sampling

The rupture plane is divided into subfaults, with their dimension calculated based on the maximum frequency ($f_{k_{\max}}$) used in simulations. The spatial sampling is limited to the Nyquist wavenumber (k_{NY}) to avoid aliasing. The Nyquist wavenumber is inversely proportional to the sub-fault size (SF_{dim}). By defining the maximum frequency as $f_{k_{\max}} \approx k_{\mathrm{NY}} \times V_R$, the required sub-fault dimension is derived as:

$$SF_{\mathrm{dim}} = \frac{V_R}{2\, f_{k_{\max}}}. \tag{5}$$

3.2 Rupture Kinematics

Following Hisada (2000, 2001), we accounted for variable rupture velocity by applying spatial perturbations to the theoretical rupture times over the rupture area according to k^{-2} decay model. The rupture time is defined as:

$$T(x,y) = \frac{D_{\text{nuc}}(x,y)}{V_R}\left(1 + \Delta T_R(x,y)\right), \tag{6}$$

where $D_{\text{nuc}}(x,y)$ is the distance from the nucleation point to the subfault located at position (x,y) on the fault, and $\Delta T_R(x,y)$ denotes the rupture-time variation, expressed in percentage, representing the maximum roughness of the propagation front. The characteristic dimensions of $\Delta T_R(x,y)$ vary between 30% and 70% of the fault length and width. Its amplitude spectrum, $\Delta T_k(k_x,k_y)$, over the fault plane is defined as (Hisada 2001):

$$\Delta T_k(k_x,k_y) = \frac{1}{\sqrt{1 + \left[\left(\frac{k_x}{k_{cTx}}\right)^2 + \left(\frac{k_y}{k_{cTy}}\right)^2\right]^2}}, \tag{7}$$

where k_{cTx} and k_{cTy} are the corner wavenumbers along strike and dip, respectively. The slip-rate function is defined according to the model proposed by Hisada (2001). This formulation relies on two characteristic frequencies: $f_1 = 1/(2\tau_{\text{rise}})$ and $f_{\max} = 1/\tau_1$, where τ_{rise} is the rise time (slip-rate function duration) and τ_1 is the duration of the triangular pulse. The rise time is derived from the seismic moment (M_0) using the following relationship (Somerville et al. 1999):

$$\tau_{\text{rise}} = 2.03 \times 10^{-9}\,(M_0)^{1/3}, \tag{8}$$

where M_0 is in dyne $\cdot$ cm.

Finally, we obtain the absolute source time function, or moment rate function $\dot{M}_0(t)$, by integrating the contributions from each sub-fault on the fault plane as:

$$\dot{M}_0(t) = \mu \int_0^L \int_0^W D(x,y) \times \left[\text{SRF}(t) * \delta\big(t - T(x,y)\big)\right] \mathrm{d}x\,\mathrm{d}y, \tag{9}$$

where the coordinates x and y denote the along-strike and along-dip directions, respectively, $D(x,y)$ is the static slip, and $\text{SRF}(t)$ is the normalized slip-rate function of time. The star symbol $(*)$ denotes the convolution operation.

3.3 Time Series Generation

According to the discrete representation theorem, the simulated acceleration $U(\vec{r},t)$ at a station located at position $\vec{r}$ can be expressed as (Aki and Richards 2002):

$$U(\vec{r},t) = \int_0^L \int_0^W R(x,y;t) \cdot \text{FG}_{x,y}(\vec{r},t)\,\mathrm{d}x\,\mathrm{d}y, \tag{10}$$

where $R(x,y;t)$ denotes the contribution to the position-dependent moment rate function at the sub-fault located at (x,y), while $\text{FG}_{x,y}(\vec{r},t)$ represents the corresponding acceleration Green's function associated with the same sub-fault. Since distinct EGFs are not available for every individual sub-fault, we approximate $\text{FG}_{x,y}(\vec{r},t)$ at position (x,y) using the closest available EGF, $\text{FG}_0(\vec{r},t)$. The Empirical Green's Function is deconvolved from its source spectrum so that it can be used as a Green's function. The amplitude source spectrum $S(m_o,f_c)$ is approximated using the ω^{-2} model of Brune (1970) as:

$$S(m_0,f_c) = \frac{m_0}{1 + \left(\frac{f}{f_c}\right)^2}, \tag{11}$$

where m_o is moment magnitude. A correction for time shift is applied to the Green's function $\text{FG}_0(\vec{r},t)$ using the relation:

$$\Delta t(x,y) = \frac{R^{\text{SF}_{x,y}}_{\text{STA}(\vec{r})} - R^{\text{SG}_0}_{\text{STA}(\vec{r})}}{V_s}, \tag{12}$$

where $R^{\text{SF}_{x,y}}_{\text{STA}(\vec{r})}$represents the distance between considered station and the sub-fault located at (x,y) within the rupture area and $R^{\text{SG}_0}_{\text{STA}(\vec{r})}$ represents the distance between the same station and the initial Green's function. After incorporating the effects of the geometrical spreading factor (γ), along with the frequency-dependent anelastic attenuation $Q(f)$, the final corrected Green's

function can be written as follows :

$$\begin{aligned} \mathrm{FG}^{\mathrm{adj}}_{x,y} = \mathcal{F}^{-1}\Bigg[\mathcal{F}\Bigg(& \\ & \mathrm{FG}_0(\vec{r},t) * \delta\big(t-\Delta t(x,y)\big) \\ & \cdot \left(\frac{R^{\mathrm{SG}_0}_{\mathrm{STA}(\vec{r})}}{R^{\mathrm{SF}_{x,y}}_{\mathrm{STA}(\vec{r})}}\right)^{\gamma}\Bigg) \\ & \cdot \exp\left(-\frac{\pi f\,\Delta t(x,y)}{Q(f)}\right)\Bigg], \end{aligned} \tag{13}$$

where $\mathcal{F}$ represents the fast Fourier transform, while $\mathcal{F}^{-1}$ its inverse. Finally, the Green's function is modified by applying the radiation-pattern correction proposed by Pitarka (2000) in the frequency domain. The Green's function is expressed in a spherical coordinate system (r,θ,ϕ) which is obtained from the original ENZ coordinate system using the coordinate transformation method of Aki and Richards (2002). The radiation pattern corrected Green's function is expressed as Dujardin et al. (2020):

$$\mathrm{FG}^{\mathrm{adj}}_{r,\theta,\phi} = \mathcal{F}^{-1}\left(\mathcal{F}(\mathrm{FG}_{r,\theta,\phi}) \cdot \mathrm{RPC}_{r,\theta,\phi}\right), \tag{14}$$

where $\mathrm{RPC}_{r,\theta,\phi}$ denotes the radiation-pattern correction factor, defined as:

$$\mathrm{RPC}_{r,\theta,\phi} = \begin{cases} A^{r,\theta,\phi}, & f < 1\,\mathrm{Hz}, \\ \dfrac{A^{r,\theta,\phi}-1}{3-1}\cdot(f-1)\cdot A^{r,\theta,\phi} & 1 \le f \le 3\,\mathrm{Hz}, \\ 1, & f \ge 3\,\mathrm{Hz}. \end{cases} \tag{15}$$

where $A^{r,\theta,\phi}$ is the radiation pattern correction coefficient (see Dujardin et al. (2020) for details). Finally, we rotate the Green's function back into the ENZ coordinate system using the strike, dip and rake angles of the (i,j) sub-fault along with its relative location with respect to the recording station defined in the spherical coordinate system (θ_{ij} and ϕ_{ij}) as:

$$\begin{aligned} \mathrm{FG}_{r,\theta,\phi} = {} & \mathrm{ROT}_{\mathrm{strike}_{ij}} \cdot \mathrm{ROT}_{\mathrm{dip}_{ij}} \\ & \cdot \mathrm{ROT}_{\mathrm{rake}_{ij}}\Bigg(\mathrm{ROT}_{\theta_{ij}} \cdot \mathrm{ROT}_{\phi_{ij}} \\ & \cdot \begin{pmatrix} \mathrm{FG}^{\mathrm{adj}}_{\phi} \\ \mathrm{FG}^{\mathrm{adj}}_{r} \\ \mathrm{FG}^{\mathrm{adj}}_{\theta} \end{pmatrix}\Bigg), \end{aligned} \tag{16}$$

where ROT denotes the rotated transformation matrix for planar rotation with an angle of rotation defined in (Eq. 16) above. Through this transformation matrix, we shift EGFs from their original location to sample the fault.

3.4 Selection of Simulation Parameters

The focal mechanism of the 2019 Ridgecrest earthquake is taken from the Southern California Seismic Network (SCSN) catalog. Table 2 lists all the metadata for both sets of EGFs used in this study. We have used $V_s = 3500$ m/s for the time shift correction (Eq. 12), $\gamma = 1.0$ for geometrical spreading correction and $Q_0 = 59$ and $\alpha = 1$ for anelastic attenuation correction (Eq. 13) (Eulenfeld and Wegler 2017). The radiation pattern correction (RPC) of Eq. 15 is scale-dependent: RPC = 1 for $f \ge 3$Hz with a linear transition between 1 and 3 Hz, and takes its azimuthal value below 1 Hz. The correction is applied identically to both EGF sets across the entire frequency band.

3.5 Ground-motion model comparison and residual analysis

The simulated RotD50 PGA values were compared with the median predictions from BSSA14 (Boore et al. 2014), CB14 (Campbell and Bozorgnia 2014), and CY14 (Chiou and Youngs 2014). For ground-motion model m and simulation i, the residual was defined in natural-logarithmic units as:

$$r_{m,i} = \ln\left(\frac{\mathrm{PGA}_{\mathrm{sim},i}}{\mathrm{PGA}_{m,i}}\right), \tag{17}$$

where $\mathrm{PGA}_{\mathrm{sim},i}$ is the simulated RotD50 PGA and $\mathrm{PGA}_{m,i}$ is the corresponding GMM median prediction. Positive residuals indicate simulated

amplitudes above the GMM median, whereas negative residuals indicate amplitudes below the median prediction. For each station, EGF set, and GMM, the residual distribution was characterized by its mean and population standard deviation (see Appendix A).

The influence of EGF selection was evaluated using matched realizations from Set 1 and Set 2. For each pair, the ratio of their PGA defined by

$$\Delta_i = \ln\left(\frac{\mathrm{PGA}_{\mathrm{Set}\,2,i}}{\mathrm{PGA}_{\mathrm{Set}\,1,i}}\right), \tag{18}$$

and the overall change between the two EGF sets was expressed as

$$F_{2/1} = \exp\left(\overline{\Delta}\right), \qquad \overline{\Delta} = \frac{1}{N}\sum_{i=1}^{N}\Delta_i, \tag{19}$$

where $N = 20$ is the number of matched realizations. Thus, $F_{2/1} > 1$ indicates larger simulated PGA for Set 2, whereas $F_{2/1} < 1$ indicates smaller PGA for Set 2.

The matched Set 1 and Set 2 simulations use the same source realization and GMM input parameters; therefore, $\Delta_i = r^{(2)}_{m,i} - r^{(1)}_{m,i}$. Uncertainty in $F_{2/1}$ was estimated using a paired nonparametric bootstrap, with percentile 95% confidence intervals obtained from resampled paired realizations. Further statistical details are given in Appendix A.

Possible distance dependence of the residuals was examined using BSSA14 as the primary reference model. Pearson and Spearman correlation coefficients were calculated for each station and EGF set, with bootstrap confidence intervals used to evaluate their uncertainty. The same analysis was repeated using CB14 and CY14 residuals as a sensitivity check; the corresponding statistics are provided in Table S2 of the supplementary materials.

4 Fault Geometry

While the source is approximated as a single fault plane with an average northwest trend of 322° (Barnhart et al. 2019; Ross et al. 2019), we adopted here a more rigorous 3-D fault model with significant along-strike curvature and depth-dependent dip variations. We defined the fault surface geometry, following the high-fidelity finite element constraints of Tung et al. (2021), as 67 km in length and 25 km in width with a curvilinear surface.

The along-strike variation is not uniform; it initiates from 322° in the south, with a distinct eastward bend of ∼340° near the epicenter, and curves back westward at the north terminus, consistent with the surface rupture. For vertical variation, we accounted for the "tulip structure" complexity (Wang and Zhan 2020), where shallow distributed faults converge into a simple, steep fault at depths deeper than 5 km. As a result, the dip angle varies spatially, transitioning from complex shallow geometry to a stable 84° eastward dip, while also capturing the localized rotation toward near-vertical structures in the southern segment (Figure 3). Further, the fault is divided into sub-faults to ensure that our simulation results capture frequencies of ground motion up to $f_{kmax} = 15$ Hz. Thus, according to Eq. 5, the size of the sub-fault is set to $SF_{dim} = 80$ m.

5 Ground motion variability

The ground motion simulation is performed for the 2019 Ridgecrest (M_w 7.1) event by varying source and rupture parameters. The parameters for each simulation are listed in supplementary Table S1. The theoretical corner frequency that depends on estimate of stress drop is used to calculate the corner wavenumber k_c. The stress drop is the key earthquake source parameter that determines magnitude of ground motion. Variation in stress drop is used to constrain the ground motion variability defined by lognormal distribution having a mean $\Delta\sigma = 1.55$ MPa and standard deviation of 0.25. Rupture velocity V_r varies from $0.7 \times V_s$ to $0.85 \times V_s$ (Heaton 1990). Further, its value is defined between these estimates with a uniform distribution. A minimum V_r of 2451.2 m/s and a maximum V_r of 2963.3 m/s are considered from simulations. Equations (6,7) control the rupture-time variation by adding a perturbation to the rupture-time, with its shape governed by the corner wavenumber.

The rupture-times are varied randomly between 30% and 70% of L and W, respectively and are normalized so that they do not exceed 20% of the theoretical value. The nucleation point of the earthquake is selected according to Mai

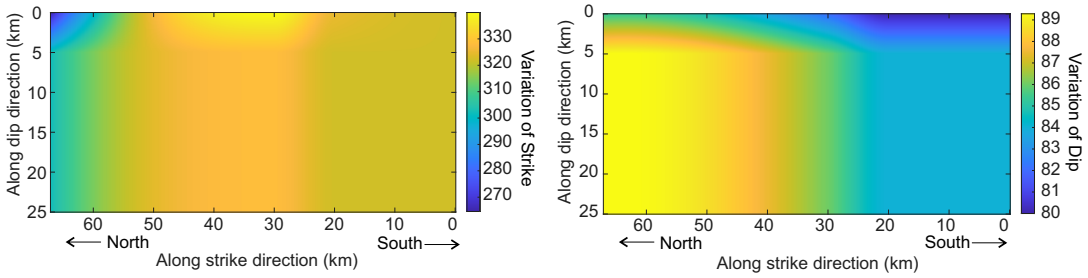


Fig. 3 Variations in strike and dip along the modeled Eastern Little Lake fault associated with the 2019 Ridgecrest (M_w 7.1) earthquake mainshock. The horizontal axis represents the along-strike distance (0–67 km), extending from south to north, while the vertical axis represents the down-dip distance (0–25 km). The color bars indicate the variation of strike and dip angles (in degrees), respectively

et al. (2005), which is set in the deepest half of the rupture area (Figure 4). Each simulation is performed by varying the static slip, nucleation position and the perturbation of the rupture velocity. The absolute source time functions follow the ω^{-2} Brune's model (Brune 1970).

The estimates of rupture velocity and stress drop are used to determine the rupture dimensions in each simulated scenario, which vary between $L \times W = 39.44 \times 14.72$ km^2 and $L \times W = 58.64 \times 21.92$ km^2 (Figure 5). The source variability depends on the position of the rupture area on the defined fault surface, which is defined on the southern segment of the fault, aligning with the dominant south-eastward directivity (Hirakawa and Barbour 2020) and the zone of maximum surface slip.

6 Results

The simulated ground motions were first examined in terms of PGA versus source-receiver distance and were subsequently compared with empirical ground-motion models. We conducted 20 simulations for each of the four stations using two sets of EGFs by varying the source parameters, as introduced in the model (Table S1). A band-pass filter (1-15 Hz) is applied to the simulation results. As for the source realizations, variations in rupture dimensions and position produced appreciable changes in the source-to-site distance, particularly for the closest station. Figure 6 illustrates variations of geometric mean horizonatal PGA with distance for CLC and CCC with EGF Set 1. At CLC, R_{JB} ranges from 1.29 to 16.55 km, R_{hyp} from 26.69 to 51.50 km and R_{rup} from 3.20 to 16.75 km. The corresponding ranges at CCC are 34.71–54.92 km, 64.75–89.44 km, and 34.71–54.94 km, respectively. These results show that the source-to-site geometry varies appreciably between realizations rather than being represented by a single distance for each station. The simulated PGAs at CLC are dispersed more than those at CCC, which are in agreement with the scatter in the source-to-site geometry.

For each simulation, PGA is calculated from the orthogonal horizontal components (North-South and East-West) using the RotD50 metric, which corresponds to the median peak amplitude obtained after rotating the acceleration time histories through all azimuths (0° to 180°) and is plotted against the Joyner-Boore distance (R_{jb}). The simulated RotD50 PGA values are compared with the median predictions of the BSSA14, CB14, and CY14 GMMs for stations CLC (hard rock), GSC (hard rock), CCC (soft rock) and SRT (alluvium) using two independent EGF sets (Figure 7). The comparison reveals a consistent station-dependent pattern across the three GMMs. The corresponding simulation-to-GMM ratios for all three models are shown in supplementary Figure S2. For a given realization, the three GMMs yield similar ratios at GSC, SRT and CCC, so the scatter in each plot arises mainly from differences in source realization. At CLC, in contrast, the ratio depend on the GMM, with BSSA14 generally giving the highest values and CB14 the lowest (Figure S2).

At the hard-rock site CLC, located about 5 km north of the mainshock on granitic rock, simulations from both EGF sets are distributed about the GMM medians and lie mostly within the $\pm 1\sigma$ bounds, with Set 2 giving relatively

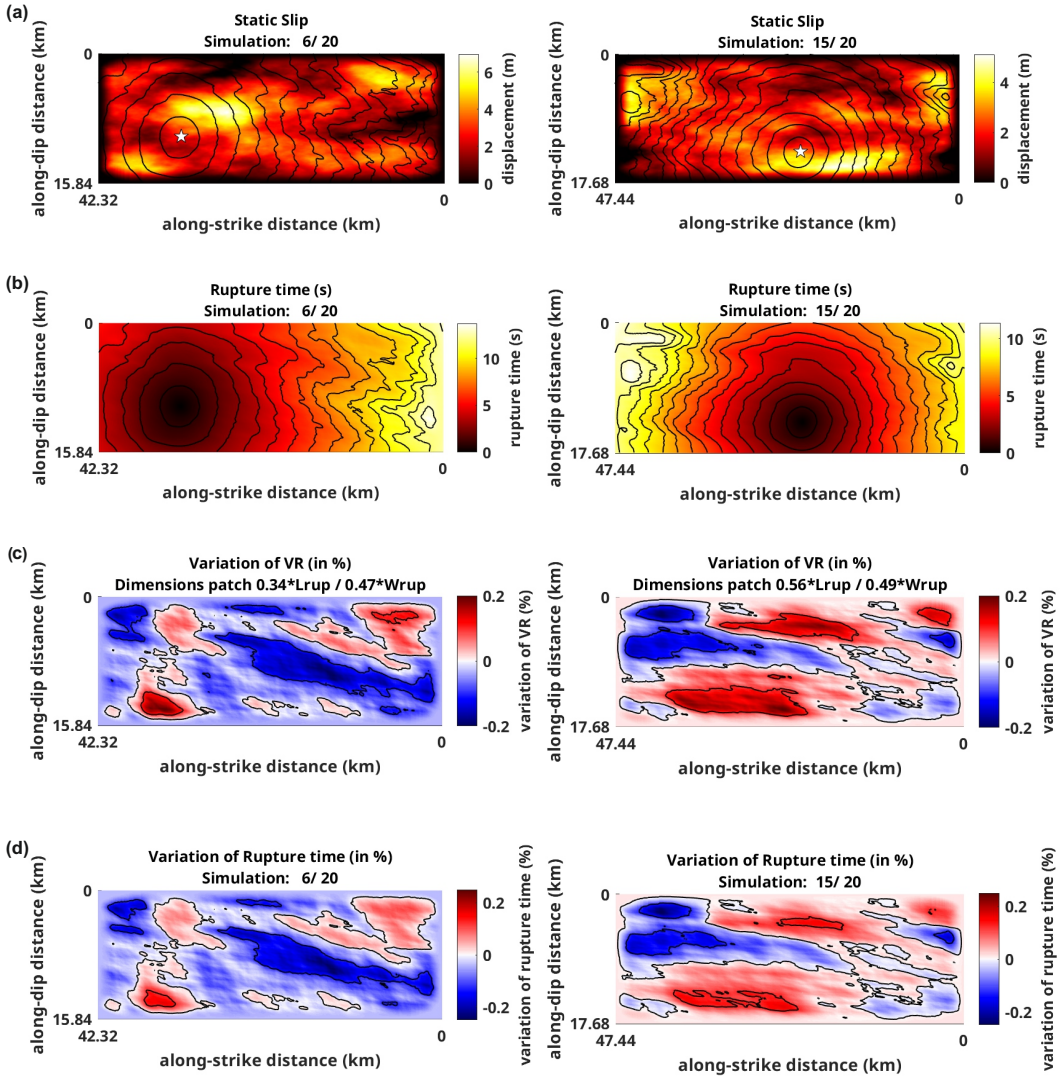


Fig. 4 Spatial distribution of kinematic source parameters for two stochastic realisations: Simulation 6 (left column) and Simulation 15 (right column). (a) Final static slip distribution (in metres), overlaid with rupture-time isochrons (black contours) originating from the nucleation point (white star). (b) Variations in rupture time (in seconds). (c) Variations in stochastic rupture-velocity (V_R), expressed as a percentage deviation from the mean velocity. (d) Percentage variation in rupture time (T_R) relative to a constant-velocity model.

larger amplitudes than Set 1 at the shortest distances ($R_{\rm JB} < 2$ km) (Figure 7a). In contrast, simulations at site GSC lie systematically below the three GMM medians, and the discrepancy is substantially larger for Set 2 (Figure 7b). At alluvium site SRT, simulations are also predominantly below the GMM medians, where both EGF sets produce broadly similar amplitude ranges (Figure 7c). At the soft-rock station CCC, the simulations lie at or above the GMM medians and are largely within the $+1\sigma$ bound, with little separation between the two EGF sets (Figure 7d). Thus, the sign and relative magnitude of the (simulation–GMM) differences are generally consistent among the ground-motion models BSSA14, CB14, and CY14, whereas the differences among

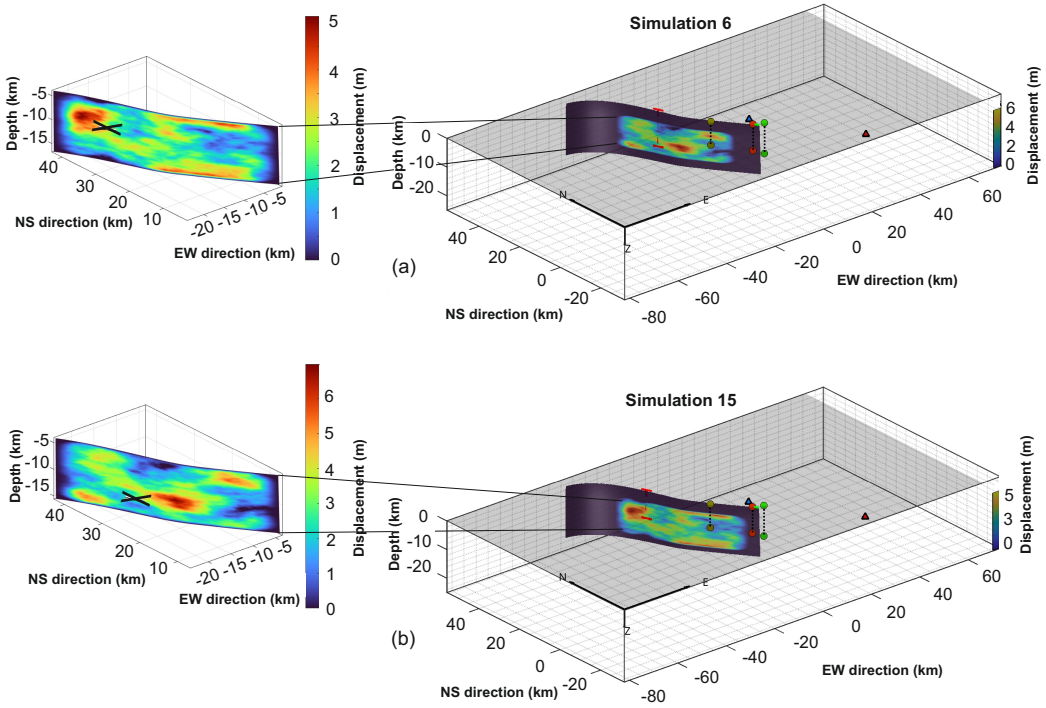


Fig. 5 Positions of rupture area on the fault plane for (a) Simulation 6 and (b) Simulation 15, at the two stations CLC and CCC. A zoomed view of the rupture plane is shown on the left for each simulation, with the cross mark indicating the nucleation point projected on the map.

stations and, especially at the hard-rock sites CLC and GSC, the difference in PGA between the EGF sets are more pronounced.

Table 3 lists the residual statistics of simulated RotD50 PGAs relative to the BSSA14, CB14, and CY14 median predictions for both EGF sets 1 and 2. At CLC, the mean residuals are close to zero for all three GMMs, ranging from −0.274 to +0.109 for Set 1 and from −0.043 to +0.339 for Set 2. The paired comparison gives geometric-mean of the Set 2/Set 1 PGA ratio, $F_{2/1} = 1.260$ with a paired-bootstrap 95% confidence interval of [1.130, 1.420], indicating systematically larger PGA for Set 2.

The largest negative residuals occur at the hard-rock site GSC that is farther away from the mainshock. Mean residuals range from −0.824 to −0.730 for Set 1 and from −1.965 to −1.871 for Set 2, depending on the GMM selected. The corresponding PGA ratio, $F_{2/1} = 0.320$ [0.291, 0.349], shows that for Set 2, simulations produce substantially smaller PGA than for Set 1. At alluvium site SRT, both EGF sets yield negative mean residuals of comparable magnitude, and $F_{2/1} = 1.062$ [0.824, 1.338]. At soft-rock site close to the mainshock, CCC, the residuals are positive for all the three GMMs analyzed and the ratio is $F_{2/1} = 0.936$ [0.845, 1.024]. The confidence intervals for SRT and CCC are close to unity, thus the difference in residual between the two EGF sets is not statistically resolved at these stations. In contrast, the PGA ratio, $F_{2/1}$ at hard-rock sites CLC and GSC deviate from unity.

The dependence of the residuals on source-receiver distance was examined using the BSSA14 GMM (Figure 8). Most station–EGF combinations show weak to moderate correlations, with the bootstrap confidence intervals close to zero. A relatively higher distance-dependence is found for SRT with EGF Set 1, where both Pearson

Table 3 Natural-log residual statistics of simulated RotD50 PGA relative to the BSSA14, CB14, and CY14 median predictions, together with the paired effect of EGF selection

Station	EGF set	N	BSSA14 $\overline{r}$ (σ_r)	CB14 $\overline{r}$ (σ_r)	CY14 $\overline{r}$ (σ_r)	$F_{2/1}$ [95% CI]
CLC	Set 1	20	+0.109 (0.301)	−0.274 (0.365)	−0.159 (0.302)	–
CLC	Set 2	20	+0.339 (0.489)	−0.043 (0.559)	+0.071 (0.497)	1.260 [1.130, 1.420]
GSC	Set 1	20	−0.730 (0.451)	−0.824 (0.509)	−0.800 (0.453)	–
GSC	Set 2	20	−1.871 (0.421)	−1.965 (0.471)	−1.940 (0.428)	0.320 [0.291, 0.349]
SRT	Set 1	20	−0.965 (0.725)	−0.848 (0.750)	−1.009 (0.714)	–
SRT	Set 2	20	−0.905 (0.374)	−0.789 (0.406)	−0.949 (0.373)	1.062 [0.824, 1.338]
CCC	Set 1	20	+0.444 (0.365)	+0.527 (0.407)	+0.477 (0.356)	–
CCC	Set 2	20	+0.378 (0.318)	+0.461 (0.358)	+0.411 (0.322)	0.936 [0.845, 1.024]

Note: Values in parentheses represent the population standard deviations of the natural-log residuals. $F_{2/1}$ denotes the ratio of the geometric-mean PGA values for Set 2 relative to Set 1 ; brackets indicate the 95% paired-bootstrap confidence interval. The paired factor is reported on the Set 2 row for each station.

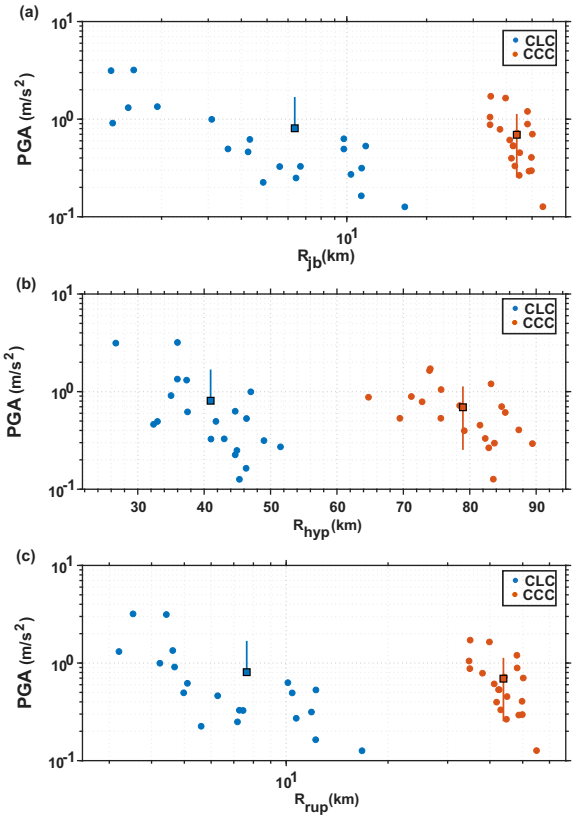


Fig. 6 Variation of simulated PGA for 20 source realizations at CLC and CCC using EGF Set 1, as a function of (a) Joyner–Boore distance (R_{JB}), (b) hypocentral distance (R_{hyp}), and (c) rupture distance (R_{rup}). Colored symbols represent individual simulations. Square symbols indicate the station-wise mean PGA values; error bars denote standard deviation

($r_p = -0.66$) and Spearman ($\rho_s = -0.69$) coefficients indicate a negative correlation between the residual and R_{JB}. The corresponding trend is weaker for SRT with EGF Set 2, and no statistically significant distance-dependence is found for CLC, GSC, or CCC. A similar pattern in distance-dependence of residuals was observed for the other two GMMs (CB14 and CY14) (see Table S2 of supplementary materials). For both models, SRT with set-1 is the only combination with a negative coefficient ($r_{\mathrm{P}} = -0.57$ and -0.59, $\rho_{\mathrm{S}} = -0.66$ and -0.68 for CB14 and CY14, respectively). For all station-set combinations, the coefficients have the same sign as BSSA14 and differ by no more than 0.11, indicating that the residual-distance pattern is robust to the choice of GMM.

7 Discussion

7.1 Comparison between EGF simulations and GMMs

A comparison of the simulated RotD50 PGAs with those from the BSSA14, CB14, and CY14 models reveals clear differences among the stations (Figure 7). Importantly, the sign and relative magnitude of the residuals are generally consistent among the three GMMs, indicating that our attenuation relation is robust across different ground motion models used. This behaviour is in agreement with previous analysis results of the Ridgecrest sequence, for which the NGA-West2 models explain the magnitude and distance-dependence

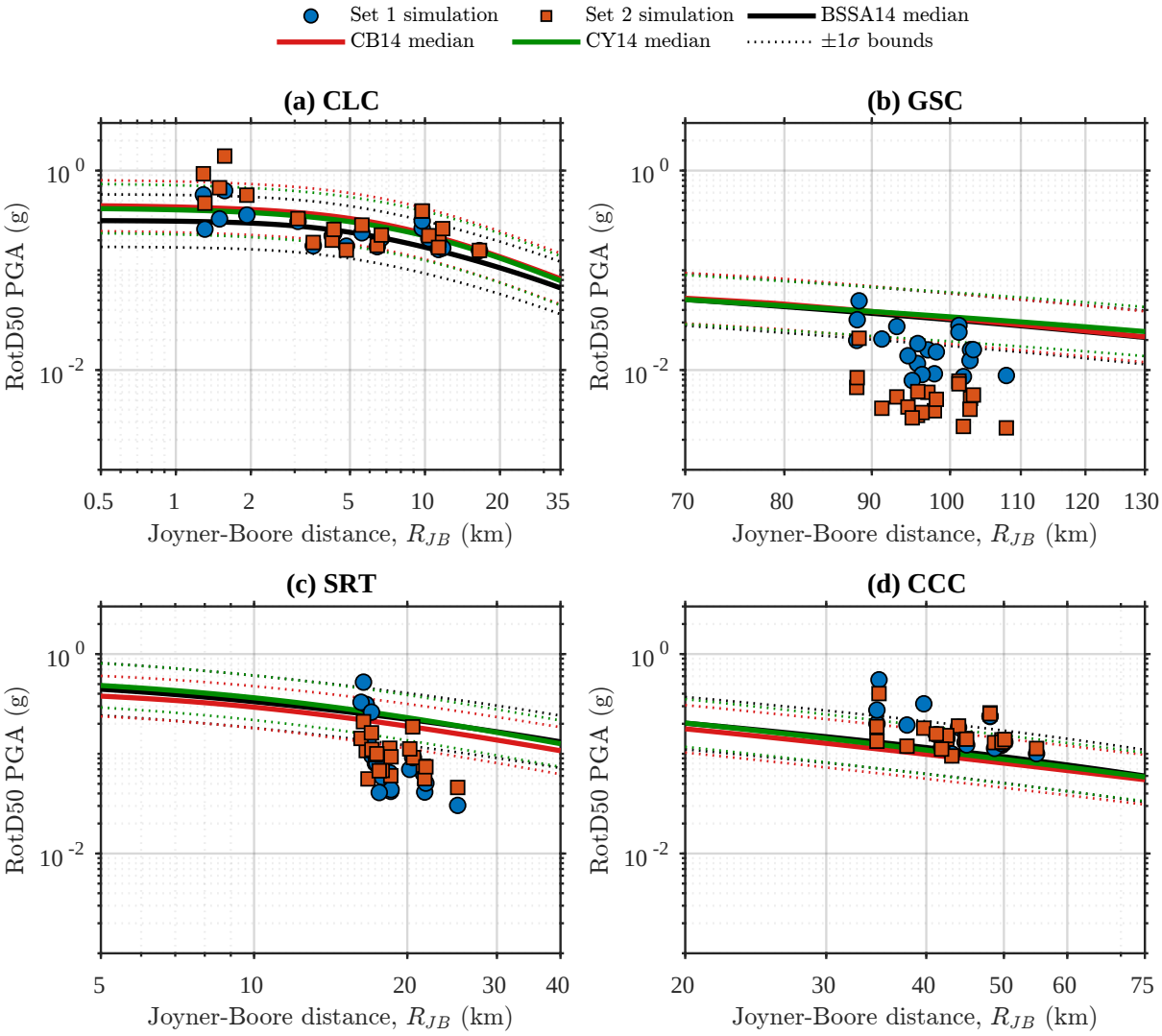


Fig. 7 Simulated RotD50 PGA as a function of Joyner–Boore distance (R_{JB}) at (a) CLC, (b) GSC, (c) SRT, and (d) CCC. Circles and squares denote the PGA estimates obtained using EGF Sets 1 and 2, respectively. Solid curves show the median predictions from BSSA14, CB14, and CY14; dotted curves indicate the corresponding exp($\pm\sigma$) bounds, where σ is the total standard deviation of each GMM in natural-log units.

of PGAs reasonably well (Ahdi et al. 2020; McNamara et al. 2020; Parker et al. 2020).

At the hard-rock station CLC ($V_{S30} \approx$ 1464 m/s), the simulated PGAs are close to the median predictions of BSSA14, CB14, and CY14 for both EGF sets (Figure 7). The corresponding residual for the EGF Set 1 is close to zero, which means that the ground motion at this site does not require station-specific calibration. The larger values of PGA obtained with Set 2 occur mainly for $R_{\mathrm{JB}} < 2$ km, where the three GMMs themselves differ by up to 0.38 in natural-log units, which is comparable to the difference in PGA between the two EGF sets, which limits the meaningful comparison between the two PGAs. The results are consistent with those of McNamara et al. (2020), who also reported that the recorded ground motions at the nearby soft-rock site CLC were not fully represented by BSSA14.

A different behaviour is obtained for the distant hard-rock site GSC, for which the simulated PGA lies below the median of all three GMMs

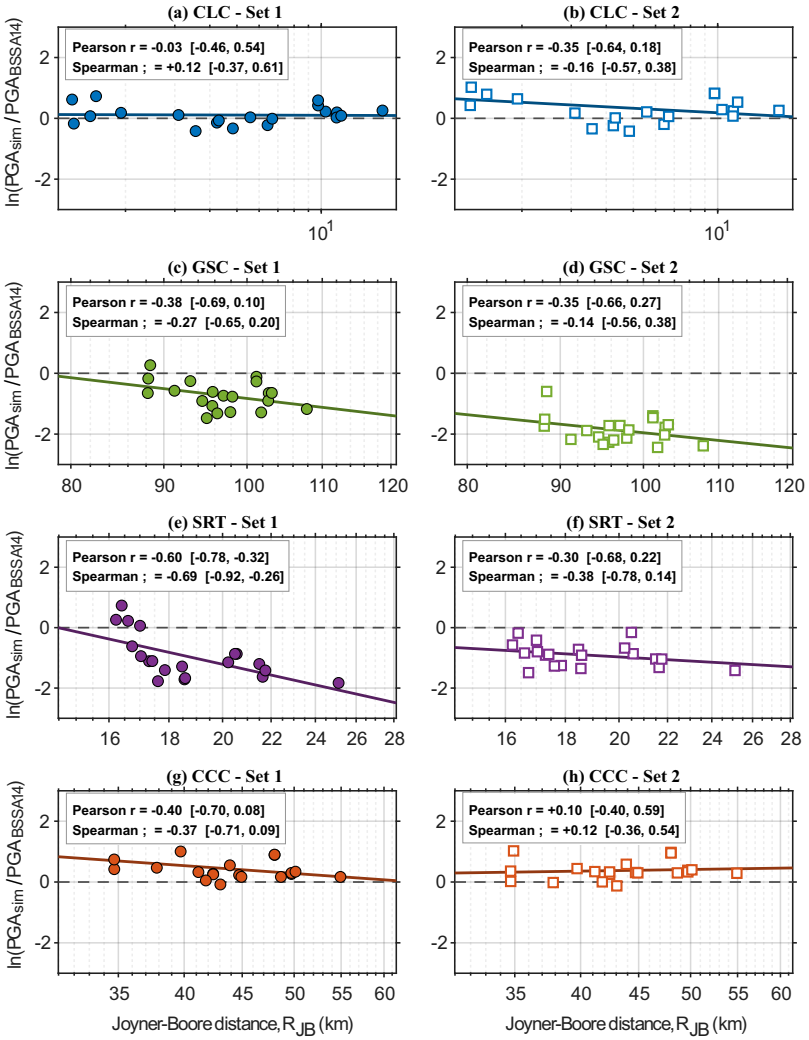


Fig. 8 Natural-log BSSA14 residuals, $r = \ln(\mathrm{PGA_{sim}}/\mathrm{PGA_{BSSA14}})$, as a function of Joyner–Boore distance (R_{JB}) for the four stations and two EGF sets. Solid lines show least-squares fits and the horizontal dashed line denotes zero residual. Each panel reports Pearson's r_p and Spearman's ρ_s correlation coefficients, together with paired-bootstrap percentile 95% confidence intervals obtained from 20 000 samples of the observed (R_{JB}, r) pairs.

for both EGF sets, with a substantially larger discrepancy for Set 2 (Figure 7). The Set 1 discrepancy could be related to a station-specific path or site contribution that the GMMs do not faithfully reproduce; the additional Set 2 discrepancy is related to the EGFs themselves and is discussed in Section 7.3. Hirakawa and Barbour (2020) obtained synthetic velocity models at GSC that exceeded the observations and attributed such difference partly to path effects not captured by their model, including possible effects of anelastic attenuation and scattering from small-scale velocity medium heterogeneity. For nearly co-located events that sample similar paths, path and site contributions are difficult to separate, as found in the 2019 event data set (Parker et al. 2020). Thus, it is possible that the deviation at GSC most

likely reflects a combination of propagation and site effects rather than a single attenuation or site effect.

At the soft-rock site CCC ($V_{S30} \approx 432$ m/s), the simulated PGA exceeds the GMM median by a factor of about 1.5 (Figure 7), with no statistically significant difference between Set 1 and Set 2 (Table 3).

At the nearby alluvial station SRT ($V_{S30} \approx 301$ m/s) in the Indian Wells Valley basin, both EGF sets produce negative residuals with respect to all three GMMs (Figure 7). In contrast to farther hard-rock station GSC, the residuals are common to both EGF sets and they are expected from simulations with the finite-source representation together with station-specific path and site effects. Hough et al. (2020) reported high-frequency (approximately above 2–3 Hz) deamplification at alluvial sites in the Indian Wells Valley. They interpreted this behaviour as due to nonlinear sediment response, as expected in sedimentary basins. McNamara et al. (2020) similarly found that BSSA14 model overpredicted the observed high-frequency response at the basin site SRT by about a factor of 2–3. The negative residuals obtained here could be attributed to reduction of high-frequency energy due to the presence of soft alluvium at SRT. Because our EGF simulations use small-event recordings, they do not faithfully reproduce the amplitude-dependent nonlinear response that may develop during strong ground-motion shaking during mainshock, and the contribution of such non-linearity cannot be quantified from the present simulations with a scope of future studies with the use of advanced physics-based simulations.

For most station–EGF combinations, the distance-dependencies of residuals on R_{JB} are statistically not significant for all three GMMs (Figure 8; Table S2). The only exception occurs for SRT with EGF Set 1, where the residual becomes more negative with increasing distance. This generally weak distance-dependence is consistent with Ahdi et al. (2020), who found that the NGA-West2 models reproduce the average ground motion attenuation relation reasonably well for the Ridgecrest events. Thus, the contrasting residual patterns among the four stations are not primarily associated with distance scaling.

7.2 Rupture directivity and its signature on ground motion

The present simulations show a clear contrast in near-source ground-motion behaviour between CCC (soft-rock) and CLC (hard-rock). The site CCC at 35–55 km from the rupture (R_{JB}) yet shows a positive residual by about a factor of 1.5, whereas CLC, at only a few kilometres from the mainshock, agrees with the GMM medians. For the recorded M_w 7.1 mainshock, Pitarka et al. (2022) similarly reported that CCC recorded larger PGA and PGV than CLC, although CLC was located closer to the fault. This difference in ground motion behavior suggests that the near-fault ground-motion amplitude is influenced by the spatial variation of the rupture in addition to the effect of site and source-receiver distance.

Previous studies show that the Ridgecrest mainshock involved a complex rupture with an important south-east-ward-propagating component (Hirakawa and Barbour 2020; Wang et al. 2020; Wu et al. 2021). The site CCC lies close to the southern end of the mainshock rupture, where rupture propagation toward the station can enhance PGA from successive parts of the fault. Baltzopoulos et al. (2020) identified a pulse-like mainshock record at CCC due to forward-directivity effect relative to CLC. The larger simulated PGA at CCC relative to the GMM medians is, therefore, consistent with a rupture-directivity contributing to the near-source ground motion. This interpretation is also compatible with the residual analysis of Ahdi et al. (2020), who showed that accounting for rupture directivity and slip heterogeneity reduced the dispersion of near-source Ridgecrest ground-motion residuals. Chu et al. (2025) identified highly heterogeneous rupture-directivity patterns among small earthquakes of the Ridgecrest sequence, further highlighting the complexity and azimuthal variability of source radiation in the region.

7.3 Sensitivity to EGF selection

On comparing the ground motions corresponding to the two EGF sets, we found that EGF selection is an important component of simulation uncertainty, but its influence varies substantially among stations (see Table 3). The strongest sensitivity occurs at the distant hard-rock station GSC,

where Set 2 gives PGA that is about one third of that obtained with Set 1. A smaller but statistically significant difference is also observed at nearby hard-rock station CLC, where Set 2 produces systematically larger PGA. In contrast, the confidence intervals for SRT (alluvium) and CCC (soft-rock) are close to unity, indicating that the difference in PGA between the two EGF sets is not statistically resolved at soft-rock and basin sites (Figure 7; Table 3). We found the EGF-effect is largest at the most distant station, where PGA can change by a factor of about three with the choice of EGF. This is expected as the signal suffers from increased attenuation of high-frequency energy with distance.

The two EGF sets differ in magnitude, corner frequency, spatial location, and focal mechanism (Table 2). In particular, event 38466343 in Set 2 has the lowest corner frequency and the largest focal-mechanism difference from the mainshock among the selected events (Table 2). Dujardin et al. (2020) emphasized the importance of EGF location, focal mechanism, and the corrections required when a limited number of EGFs are redistributed over an extended fault. Differences in focal mechanism of the EGF and that of target subfaults are corrected by radiation pattern correction, which has its largest effect at short source-receiver distance. In contrast to our results, Wu et al. (2021), however, found that the main features of their inferred Ridgecrest slip model remained stable when different EGFs were used.

7.4 Comparison with published Ridgecrest source models

Independent source models indicated substantial spatial and temporal variability during the M_w 7.1 rupture. The source model used in the current simulations is consistent with the complex and spatially variable rupture behaviour reported for the 2019 Ridgecrest mainshock. The stochastic k^{-2}–EGF formulation combines a non-planar fault geometry with variations in slip, rupture dimensions, nucleation position, and rupture velocity, thereby generating an ensemble of physically plausible source realizations. This source representation is supported by observations of the Ridgecrest sequence. As for the previous source models, Ross et al. (2019) showed that the sequence ruptured a multi-scale network of interlaced faults. Plesch et al. (2020) derived 3-D fault geometry that are non-planar and strongly constrained by relocated seismicity, focal mechanisms, and mapped surface rupture. Wang et al. (2020) inferred strong variations in slip and rupture propagation over the fault system. Using EGF waveform inversion, Wu et al. (2021) identified two principal large-slip regions with a relatively low rupture velocity. Pitarka et al. (2022) showed that incorporating depth-dependent variations in the slip-rate function improves the simulation of near-fault Ridgecrest ground motions. Trugman (2020) found systematic spatial and depth-dependent variations in stress drop throughout the Ridgecrest sequence, while Ji et al. (2025) reported comparable variations in stress drop for moderate Ridgecrest earthquakes. These studies support the use of variable stress drop within the stochastic rupture ensembles. Taken together, these studies provide independent support for representing the Ridgecrest source through spatially variable rupture properties rather than a single uniform kinematic description alongside a variable stress drop associated with the rupture emsembles, which is in agreement with our adopted source model. In this study, we sampled a range of source configurations consistent with the principal characteristics of the Ridgecrest sequence, as above and examined how this source variability influences the ground motion at different sites.

7.5 Implications for site-specific ground-motion simulation

The four stations considered here represent contrasting site conditions, and the simulation results vary accordingly. At hard- and soft-rock sites, the k^{-2}–EGF framework on a non-planar fault reproduces the median ground motion within the uncertainty of the GMMs. The two Class C stations (GSC and CCC) do not necessarily lead to similar simulation results. At GSC ($V_{S30} \approx 697$ m/s), the simulations under-predict the empirical median levels, particularly for EGF Set 2, indicating a possible influence of the selected EGFs and sampled propagation path. In contrast, CCC ($V_{S30} \approx 432$ m/s) shows systematically elevated PGA for both EGF sets, with little sensitivity to the choice of EGF selected. Thus, the source–station configuration and the propagation path sampled by the EGFs are as important as V_{S30} for site-specific

simulations. For the three GMMs considered, the within-set standard deviations of the residuals range from 0.30 to 0.56 for all combinations except for the alluvium site SRT with EGF Set 1 (0.71–0.75; Table 3), and are lower than the total standard deviation of each GMM. This is expected, because only the source varies between realizations while the path and site effect are fixed by the EGF records. The scatter in simulation results, therefore, represents the source-related variability at a given site. The EGF-choice can change the GMM median by a factor of about three at distant stations, EGF selection can be treated as a major source of uncertainty for site-specific ground-motion simulation. At basin site such as SRT, simulation captures the small-event site effect but not the non-linear response reported for the Indian Wells Valley sediments (Hough et al. 2020; McNamara et al. 2020). At such sites, the PGA estimates may require an additional treatment of nonlinear site response beyond the variability introduced through the stochastic source model. This non-linearity likely explains the departure of the within-EGF-set standard deviations of the residuals from the total standard deviation, as explained above.

7.6 Limitations and outlook

The selection of EGF was constrained by the available data set. From a catalog of Trugman (2020) 55 candidate events, only six satisfied the combined requirements of magnitude, hypocentral proximity, signal-to-noise ratio, and focal mechanism compatibility with the mainshock. Consequently, the selected EGFs were divided into two groups of three events for simulation. A larger EGF database can, however, provide a more rigorous assessment of the sensitivity of simulated ground motion to EGF selection. We have applied the low-frequency radiation pattern correction of Pitarka (2000), assuming that the source radiation is isotropic for frequencies higher than ∼3 Hz and therefore cannot compensate for residual differences resulting from high-frequency source radiation. Nozu and Nagasaka (2017) identified the same limitation for the 2016 Kumamoto earthquake sequence. We assumed that the mean rupture velocity is constant within each simulation, with its value drawn from a uniform distribution across simulations. Also, all sub-faults are assigned to the same analytical slip rate function following Hisada (2001). However, kinematic inversions of the Ridgecrest earthquake indicate substantial spatial variations in rupture velocity (Jia et al. 2020). Pitarka (2022) showed, for the Ridgecrest event, a depth-dependent slip-rate function, derived from dynamic rupture modelling. Incorporating these spatially variable rupture velocity and depth-dependent slip rate function in the current source model would further constrain the ground motion estimates. This study inherits the linear site response of the small EGF events at all recording stations, as in the standard EGF technique. This assumption is likely to fail at the alluvium (basin) station SRT, where the actual response may reflect non-linear soil behaviour (Hough et al. 2020). Furthermore, we perform simulations in the 1–15 Hz band, so long-period characteristics of ground motions are not evaluated. PGV is most sensitive to frequencies near the corner frequency of the simulated event, which for the M_w 7.1 Ridgecrest mainshock lies near 0.056 Hz, which is well below our low-frequency cutoff. This limitation could be addressed either by incorporating a velocity recording EGF or a hybrid method coupling with low-frequency ($<$ 1 Hz) 3-D numerical simulations.

8 Conclusions

We simulated the high-frequency (1–15 Hz) ground motions of the 2019 M_w 7.1 Ridgecrest mainshock at four stations on hard rock, soft rock and alluvium, using a k^{-2} kinematic source on a non-planar 3-D fault combined with two independent sets of empirical Green's functions. The simulated RotD50 PGAs were compared with those predicted by the BSSA14, CB14 and CY14 ground-motion models. The main conclusions are as follows:

1. The simulations show a clear station dependency for all the three GMMs considered. At the near-source hard-rock station CLC, the simulated PGAs are close to the GMM medians, within a factor of about 1.4. At the soft-rock station CCC, both EGF sets give positive residuals, with PGA approximately 1.5–1.7 times the GMM medians. This PGA amplification could be attributed to rupture directivity

resulting from favourable source-to-site configuration of CCC near the southern end of the rupture, as reported for the Ridgecrest mainshock.

2. At the distant hard-rock station GSC and the alluvial station SRT, the simulations are systematically below the three GMM medians. The strongest negative bias occurs for GSC for EGF Set 2, for which only 0–5% of the realizations fall within the $\pm 1\sigma$ range. At SRT, simulations for both EGF sets are negatively biased, with only about 15–25% of the simulations falling within $\pm 1\sigma$. The persistence of the basin site SRT response across both EGF sets points to wave propagation and non-linear site effects likely contributing to the simulation results.
3. EGF selection plays an important role in site-specific ground motion simulations. For hard-rock sites, EGF Set 2 gives PGA that is about one third of the Set 1 PGA at GSC ($F_{2/1} = 0.320$) and about 1.3 times the Set 1 PGA at CLC ($F_{2/1} = 1.260$), whereas the differences at basin and soft-rock sites (SRT and CCC) are not statistically resolved.
4. The within-set standard deviations of the residuals are 0.30–0.56 for all station–EGF set combinations except for the basin site SRT with EGF Set 1 (0.71–0.75), comparable to or lower than the total standard deviations of the GMMs. They likely represent the source-related variability at a fixed site. The departure at SRT could be related to the non-linear site response at basins that is not reproduced by the current GMMs.

Overall, combining a spatially variable k^{-2} rupture ensemble, a non-planar fault geometry, and radiation-corrected EGFs provides a physics-based framework for examining site-specific high-frequency ground-motion variability. Source variability alone does not explain all differences among the stations; the characteristics of the selected EGFs, path, and site effects, especially non-linear site response at sedimentary basins are important components of site-specific ground-motion prediction.

Supplementary information. Supplementary material accompanying this article is provided as Online Resource 1, containing additional figures and tables supporting the analyses presented in the main manuscript.

Acknowledgements. We acknowledge the use of open source data from the Southern California Earthquake Data Center (SCEDC). The V_{s30} values were obtained from the Center for Engineering Strong Motion Data (CESMD). Figures were prepared using the Generic Mapping Tools (PyGMT). The authors also thank IIT Roorkee for providing computational resources and infrastructure support. The authors acknowledge the use of ChatGPT (OpenAI) for language refinement and assistance with code debugging. AKM acknowledges the support of the IIT Roorkee (MHRD) fellowship for pursuing this work.

Data and Resources. The earthquake data used in this study were obtained from the Southern California Earthquake Data Center (SCEDC) (https://scedc.caltech.edu/data/stressdrop-ridgecrest.html). Station information, including V_{s30} values, was obtained from the Center for Engineering Strong Motion Data (CESMD) (https://www.strongmotioncenter.org/). Both datasets are publicly available through their respective online data repositories. Map preparation and seismic-data processing were performed using Generic Mapping Tools (GMT) and ObsPy, respectively. Ground-motion simulations and subsequent analyses were performed using MATLAB and Python.

Declarations

Funding. No funding was received for conducting this study.

Competing interests. The authors declare that they have no competing interests that are relevant to the content of this article.

Author contributions. A.K.M.: Methodology, Software, Formal analysis, Investigation, Data curation, Visualization, Writing – original draft.

S.P.: Investigation, Conceptualization, Supervision, Writing – review and editing.

Appendix A Residual statistics and bootstrap analysis

For a station–EGF combination containing N simulations, the mean residual relative to model m is

$$\overline{r}_m = \frac{1}{N}\sum_{i=1}^{N} r_{m,i}, \tag{A1}$$

and the population residual standard deviation is

$$\sigma_{r,m} = \left[\frac{1}{N}\sum_{i=1}^{N}\left(r_{m,i} - \overline{r}_m\right)^2\right]^{1/2}. \tag{A2}$$

For the paired EGF comparison, the $N = 20$ matched realization indices were resampled with replacement. For bootstrap replicate b, the mean paired logarithmic difference is denoted by $\overline{\Delta}^{*(b)}$. The 95% percentile confidence interval of the multiplicative Set 2/Set 1 factor was calculated as

$$\begin{aligned}\mathrm{CI}_{95\%}(F_{2/1}) = \big[&\exp\{Q_{0.025}(\overline{\Delta}^{*})\},\\ &\exp\{Q_{0.975}(\overline{\Delta}^{*})\}\big],\end{aligned} \tag{A3}$$

where Q_p denotes the pth quantile of the bootstrap distribution. A total of $B = 20\,000$ bootstrap resamples were used, with the same sampled indices applied to Set 1 and Set 2 so that the realization pairing was preserved.

For the residual–distance analysis, Pearson's product–moment coefficient was calculated as

$$r_{\mathrm{P}} = \frac{\sum_{i=1}^{N}(x_i - \overline{x})(y_i - \overline{y})}{\left[\sum_{i=1}^{N}(x_i - \overline{x})^2 \sum_{i=1}^{N}(y_i - \overline{y})^2\right]^{1/2}}, \tag{A4}$$

where $x_i = \log_{10}(R_{\mathrm{JB},i})$ and $y_i = r_i$.

Spearman's coefficient, ρ_{S}, was calculated as the Pearson correlation between the corresponding ranks of R_{JB} and the residuals. Since the logarithmic transformation is monotonic, the ranking of R_{JB} is unchanged by the transformation.

For both coefficients, the (R_{JB}, r) pairs were resampled together with replacement, and percentile 95% confidence intervals were obtained from the 2.5th and 97.5th percentiles of the bootstrap distributions.

References

Ahdi, S.K., Mazzoni, S., Kishida, T., Wang, P., Nweke, C.C., Kuehn, N.M., Contreras, V., Rowshandel, B., Stewart, J.P., Bozorgnia, Y.: Engineering characteristics of ground motions recorded in the 2019 ridgecrest earthquake sequence. Bulletin of the Seismological Society of America **110**(4), 1474–1494 (2020)

Aki, K., Richards, P.G.: Quantitative seismology. sausalito. Calif: University Science Books (2002)

Asano, K.: Source modeling of an m w 5.9 earthquake in the nankai trough, southwest japan, using offshore and onshore strong-motion waveform records. Bulletin of the Seismological Society of America **108**(3A), 1231–1239 (2018)

Barnhart, W.D., Hayes, G.P., Gold, R.D.: The july 2019 ridgecrest, california, earthquake sequence: Kinematics of slip and stressing in cross-fault ruptures. Geophysical Research Letters **46**(21), 11859–11867 (2019)

Baltzopoulos, G., Luzi, L., Iervolino, I.: Analysis of near-source ground motion from the 2019 ridgecrest earthquake sequence. Bulletin of the Seismological Society of America **110**(4), 1495–1505 (2020)

Brune, J.N.: Tectonic stress and the spectra of seismic shear waves from earthquakes. Journal of geophysical research **75**(26), 4997–5009 (1970)

Boore, D.M., Stewart, J.P., Seyhan, E., Atkinson, G.M.: Nga-west2 equations for predicting pga, pgv, and 5% damped psa for shallow crustal earthquakes. Earthquake Spectra **30**(3), 1057–1085 (2014)

Chen, K., Avouac, J.-P., Aati, S., Milliner, C., Zheng, F., Shi, C.: Cascading and pulse-like ruptures during the 2019 ridgecrest earthquakes

in the eastern california shear zone. Nature communications **11**(1), 22 (2020)

Campbell, K.W., Bozorgnia, Y.: Nga-west2 ground motion model for the average horizontal components of pga, pgv, and 5% damped linear acceleration response spectra. Earthquake Spectra **30**(3), 1087–1115 (2014)

Chu, S., Baltay, A., Abercrombie, R.: Characterizing directivity in small (m 2.4–5) aftershocks of the ridgecrest sequence. Bulletin of the Seismological Society of America **115**(3), 1177–1188 (2025)

Causse, M., Chaljub, E., Cotton, F., Cornou, C., Bard, P.-Y.: New approach for coupling k-2 and empirical green's functions: application to the blind prediction of broad-band ground motion in the grenoble basin. Geophysical Journal International **179**(3), 1627–1644 (2009)

Chiou, B.S.-J., Youngs, R.R.: Update of the chiou and youngs nga model for the average horizontal component of peak ground motion and response spectra. Earthquake Spectra **30**(3), 1117–1153 (2014)

Del Gaudio, S., Causse, M., Festa, G.: Broad-band strong motion simulations coupling k-square kinematic source models with empirical green's functions: the 2009 l'aquila earthquake. Geophysical Journal International **203**(1), 720–736 (2015)

Dujardin, A., Hollender, F., Causse, M., Berge-Thierry, C., Delouis, B., Foundotos, L., Ameri, G., Shible, H.: Optimization of a simulation code coupling extended source (k- 2) and empirical green's functions: Application to the case of the middle durance fault: A. dujardin et al. Pure and Applied Geophysics **177**(5), 2255–2279 (2020)

Eulenfeld, T., Wegler, U.: Crustal intrinsic and scattering attenuation of high-frequency shear waves in the contiguous united states. Journal of Geophysical Research: Solid Earth **122**(6), 4676–4690 (2017)

Graves, R.W.: Simulating seismic wave propagation in 3d elastic media using staggered-grid finite differences. Bulletin of the seismological society of America **86**(4), 1091–1106 (1996)

Hanks, T.C.: b values and ω- γ seismic source models: Implications for tectonic stress variations along active crustal fault zones and the estimation of high-frequency strong ground motion. Journal of Geophysical Research: Solid Earth **84**(B5), 2235–2242 (1979)

Hartzell, S.H.: Earthquake aftershocks as green's functions. Geophysical Research Letters **5**(1), 1–4 (1978)

Herrero, A., Bernard, P.: A kinematic self-similar rupture process for earthquakes. Bulletin of the Seismological Society of America **84**(4), 1216–1228 (1994)

Hirakawa, E., Barbour, A.J.: Kinematic rupture and 3d wave propagation simulations of the 2019 m w 7.1 ridgecrest, california, earthquake. Bulletin of the Seismological Society of America **110**(4), 1644–1659 (2020)

Heaton, T.H.: Evidence for and implications of self-healing pulses of slip in earthquake rupture. Physics of the Earth and Planetary Interiors **64**(1), 1–20 (1990)

Hisada, Y.: A theoretical omega-square model considering the spatial variation in slip and rupture velocity. Bulletin of the Seismological Society of America **90**(2), 387–400 (2000)

Hisada, Y.: A theoretical omega-square model considering spatial variation in slip and rupture velocity. part 2: Case for a two-dimensional source model. Bulletin of the Seismological Society of America **91**(4), 651–666 (2001)

Hough, S.E., Thompson, E., Parker, G.A., Graves, R.W., Hudnut, K.W., Patton, J., Dawson, T., Ladinsky, T., Oskin, M., Sirorattanakul, K., *et al.*: Near-field ground motions from the july 2019 ridgecrest, california, earthquake sequence. Seismological Research Letters **91**(3), 1542–1555 (2020)

Hutchings, L.: Kinematic earthquake models and synthesized ground motion using empirical green's functions. Bulletin of the Seismological

Society of America **84**(4), 1028–1050 (1994)

Hutchings, L., Wu, F.: Empirical green's functions from small earthquakes: a waveform study of locally recorded aftershocks of the 1971 san fernando earthquake. Journal of Geophysical Research: Solid Earth **95**(B2), 1187–1214 (1990)

Irikura, K., Kamae, K.: Estimation of strong ground motion in broad-frequency band based on a seismic source scaling model and an empirical green's function technique. Annals of Geophysics **37**(6) (1994)

Irikura, K.: Semi-empirical estimation of strong ground motions during large earthquakes. Bulletin of the Disaster Prevention Research Institute. **33** (1983)

Irikura, K.: Prediction of strong acceleration motion using empirical green's function. In: Proc. 7th Japan Earthq. Eng. Symp, vol. 151, pp. 151–156 (1986)

Ji, C., Archuleta, R.J., Peyton, A.: Capturing broadband spectral characteristics of moderate-size earthquakes using nearby recordings: A case study of 42 m w 4.0–5.4 ridgecrest earthquakes. Bulletin of the Seismological Society of America **115**(3), 850–874 (2025)

Joyner, W.B., Boore, D.M.: On simulating large earthquakes by green's–function addition of smaller earthquakes. Earthquake source mechanics **37**, 269–274 (1986)

Jia, Z., Wang, X., Zhan, Z.: Multifault models of the 2019 ridgecrest sequence highlight complementary slip and fault junction instability. Geophysical Research Letters **47**(17), 2020–089802 (2020)

Kamae, K., Irikura, K., Pitarka, A.: A technique for simulating strong ground motion using hybrid green's function. Bulletin of the Seismological Society of America **88**(2), 357–367 (1998)

Konno, K., Ohmachi, T.: Ground-motion characteristics estimated from spectral ratio between horizontal and vertical components of microtremor. Bulletin of the Seismological Society of America **88**(1), 228–241 (1998)

Kohrs-Sansorny, C., Courboulex, F., Bour, M., Deschamps, A.: A two-stage method for ground-motion simulation using stochastic summation of small earthquakes. Bulletin of the Seismological Society of America **95**(4), 1387–1400 (2005)

McNamara, D.E., G. Wolin, E.L., Moschetti, M.P., Thompson, E.M., Powers, P.M., Shumway, A.M., Petersen, M.D., Wilson, D.C., Benz, H.M.: Evaluation of ground-motion models for usgs seismic hazard models using near-source instrumental ground-motion recordings of the ridgecrest, california, earthquake sequence. Bulletin of the Seismological Society of America **110**(4), 1517–1529 (2020)

Mai, P.M., Spudich, P., Boatwright, J.: Hypocenter locations in finite-source rupture models. Bulletin of the Seismological Society of America **95**(3), 965–980 (2005)

Nozu, A., Nagasaka, Y.: Rupture process of the main shock of the 2016 kumamoto earthquake with special reference to damaging ground motions: waveform inversion with empirical green's functions. Earth, Planets and Space **69**(1), 22 (2017)

Ordaz, M., Arboleda, J., Singh, S.K.: A scheme of random summation of an empirical green's function to estimate ground motions from future large earthquakes. Bulletin of the Seismological Society of America **85**(6), 1635–1647 (1995)

Parker, G.A., Baltay, A.S., Rekoske, J., Thompson, E.M.: Repeatable source, path, and site effects from the 2019 m 7.1 ridgecrest earthquake sequence. Bulletin of the Seismological Society of America **110**(4), 1530–1548 (2020)

Pitarka, A., Graves, R., Irikura, K., Miyakoshi, K., Wu, C., Kawase, H., Rodgers, A., McCallen, D.: Refinements to the graves–pitarka kinematic rupture generator, including a dynamically consistent slip-rate function, applied to the 2019 m w 7.1 ridgecrest earthquake. Bulletin of the Seismological Society of America **112**(1), 287–306 (2022)

Pitarka, A., Somerville, P., Fukushima, Y., Uetake, T., Irikura, K.: Simulation of near-fault strong-ground motion using hybrid green's functions. Bulletin of the Seismological Society of America **90**(3), 566–586 (2000)

Plesch, A., Shaw, J.H., Ross, Z.E., Hauksson, E.: Detailed 3d fault representations for the 2019 ridgecrest, california, earthquake sequence. Bulletin of the Seismological Society of America **110**(4), 1818–1831 (2020)

Ross, Z.E., Idini, B., Jia, Z., Stephenson, O.L., Zhong, M., Wang, X., Zhan, Z., Simons, M., Fielding, E.J., Yun, S.-H., *et al.*: Hierarchical interlocked orthogonal faulting in the 2019 ridgecrest earthquake sequence. Science **366**(6463), 346–351 (2019)

Shomali, Z.H.: Empirical green's functions calculated from the inversion of earthquake radiation patterns. Geophysical Journal International **144**(3), 647–655 (2001)

Somerville, P., Irikura, K., Graves, R., Sawada, S., Wald, D., Abrahamson, N., Iwasaki, Y., Kagawa, T., Smith, N., Kowada, A.: Characterizing crustal earthquake slip models for the prediction of strong ground motion. Seismological Research Letters **70**(1), 59–80 (1999)

Trugman, D.T.: Stress-drop and source scaling of the 2019 ridgecrest, california, earthquake sequence. Bulletin of the Seismological Society of America **110**(4), 1859–1871 (2020)

Tung, S., Shirzaei, M., Ojha, C., Pepe, A., Liu, Z.: Structural controls over the 2019 ridgecrest earthquake sequence investigated by high-fidelity elastic models of 3d velocity structures. Journal of Geophysical Research: Solid Earth **126**(7), 2020–021124 (2021)

Wang, K., Dreger, D.S., Tinti, E., Bürgmann, R., Taira, T.: Rupture process of the 2019 ridgecrest, california m w 6.4 foreshock and m w 7.1 earthquake constrained by seismic and geodetic data. Bulletin of the Seismological Society of America **110**(4), 1603–1626 (2020)

Wennerberg, L.: Stochastic summation of empirical green's functions. Bulletin of the Seismological Society of America **80**(6A), 1418–1432 (1990)

Wu, S.-L., Nozu, A., Nagasaka, Y.: Rupture process of the mainshock of the 2019 ridgecrest earthquake sequence from waveform inversion with empirical green's functions. Bulletin of the Seismological Society of America **111**(2), 1014–1031 (2021)

Wang, H., Wen, R., Ren, Y.: Simulating ground-motion directivity using stochastic empirical green's function method. Bulletin of the Seismological Society of America **107**(1), 359–371 (2017)

Wang, X., Zhan, Z.: Seismotectonics and fault geometries of the 2019 ridgecrest sequence: Insight from aftershock moment tensor catalog using 3-d green's functions. Journal of Geophysical Research: Solid Earth **125**(5), 2020–019577 (2020)

Yong, A., Thompson, E.M., Wald, D.J., Knudsen, K.L., Odum, J.K., Stephenson, W.J., Haefner, S.: Compilation of v s30 data for the united states. Data Series (2016)

Supplementary Files

This is a list of supplementary files associated with this preprint. Click to download.

- ESM1.pdf